



# Matrix-specific mechanism of Fe ion release from laser-generated 3D-printable nanoparticle-polymer composites and their protein adsorption properties

Yaya Li<sup>1</sup>, Christoph Rehbock<sup>1</sup>, Milen Nachev<sup>2,3</sup>, Jacqueline Stamm<sup>4,5</sup>, Bernd Sures<sup>2,3</sup> , Andreas Blaeser<sup>4,5</sup> and Stephan Barcikowski<sup>1</sup> 

<sup>1</sup> Technical Chemistry I and Center for Nanointegration Duisburg-Essen (CENIDE), University of Duisburg-Essen, Universitätsstr. 5-7, Essen 45141, Germany

<sup>2</sup> Aquatic Ecology, University of Duisburg-Essen, Universitätsstr. 5, Essen 45141, Germany

<sup>3</sup> Center for Water and Environmental Research, University of Duisburg-Essen, Universitätsstr. 5, Essen 45141, Germany

<sup>4</sup> Institute for BioMedical Printing Technology, Technical University of Darmstadt, Magdalenenstraße 2, Darmstadt 64289, Germany

<sup>5</sup> Center for Synthetic Biology, Technical University of Darmstadt, Rundeturmstrasse 2, Darmstadt 64283, Germany

E-mail: [stephan.barcikowski@uni-due.de](mailto:stephan.barcikowski@uni-due.de)

Received 9 March 2020, revised 9 April 2020

Accepted for publication 20 May 2020

Published 14 July 2020



## Abstract

Nanocomposites have been widely applied in medical device fabrication and tissue-engineering applications. In this context, the release of metal ions as well as protein adsorption capacity are hypothesized to be two key processes directing nanocomposite-cell interactions. The objective of this study is to understand the polymer-matrix effects on ion release kinetics and their relations with protein adsorption. Laser ablation in macromolecule solutions was employed for synthesizing Au and Fe nanoparticle-loaded nanocomposites based on thermoplastic polyurethane (TPU) and alginate. Confocal microscopy revealed a three-dimensional homogeneous dispersion of laser-generated nanoparticles in the polymer. The physicochemical properties revealed a pronounced dependence upon embedding of Fe and Au nanoparticles in both polymer matrices. Interestingly, the total Fe ion concentration released from alginate gels under static conditions decreased with increasing mass loadings, a phenomenon only found in the Fe-alginate system and not in the Cu/Zn-alginate and Fe-TPU control system (where the effects were proportional to the nanoparticle load). A detailed mechanistic examination of iron ion release process revealed that it is probably not the redox potential of metals and diffusion of metal ions alone, but also the solubility of nano-metal oxides and affinity of metal ions for alginate that lead to the special release behaviors of iron ions from alginate gels. The amount of adsorbed bovine serum albumin (BSA) and collagen I on the surface of both the alginate and TPU composites was significantly increased in contrast to the unloaded control



Original content from this work may be used under the terms of the [Creative Commons Attribution 4.0 licence](https://creativecommons.org/licenses/by/4.0/). Any further distribution of this work must maintain attribution to the author(s) and the title of the work, journal citation and DOI.

polymers and could be correlated with the concentration of released Fe ions and the porosity of composites, but was independent of the global surface charge. Interestingly, these effects were already highly pronounced at minute loadings with Fe nanoparticles down to 200 ppm. Moreover, the laser-generated Fe or Au nanoparticle-loaded alginate composites were shown to be a suitable bioink for 3D printing. These findings are potentially relevant for ion-sensitive bio-responses in cell differentiation, endothelialisation, vascularisation, or wound healing.

Supplementary material for this article is available [online](#)

Keywords: laser ablation in liquid, nanocomposites, ion release kinetics, protein adsorption, 3D printing

(Some figures may appear in colour only in the online journal)

## 1. Introduction

Nanocomposites are highly interesting for biomedicine as the embedded nanoparticles can add novel functionality to the polymer. Alginate is a water-soluble biopolymer that easily forms a stable gel network in case cations like  $\text{Ca}^{2+}$ ,  $\text{Cu}^{2+}$ , or  $\text{Zn}^{2+}$  are present as cross-linkers [1]. Due to its good cytocompatibility, it has been broadly applied in tissue engineering [2, 3], however cellular adhesion in the absence of additional functional ligands is limited. To compensate for the disadvantage of lacking cell adhesion ligands, nanoparticles can be embedded into alginate to achieve the expected positive results [4]. Thermoplastic polyurethane (TPU), a medium-hardness polymer, has been applied in biomedical devices [5]. Both alginate and TPU are used as matrix materials in additive manufacturing [3, 6]. Nanoparticle-TPU or alginate composites are usually prepared by chemical methods but impurities from chemical additives as well as impaired particle stability in the polymer matrix are serious drawbacks. Composite preparation by *in situ* laser ablation in liquids could overcome these two limitations and has been discussed in our previous work [7, 8], including scalability to a high technology readiness level [8]. Potential applications of such ion-loaded nanoparticle-embedded polymers are e.g. skeletal muscle tissue engineering [9], wound healing [10], and implant materials [11]. Furthermore, previous studies demonstrated that the embedding of metal nanoparticles into alginate and TPU significantly affects the biological response, which was attributed to different mechanisms. Benign effects on cellular viability and proliferation of endothelial cells were demonstrated when insoluble nanoparticles like Pt and Au were embedded into TPU, using an *in situ* laser ablation in liquids approach. Here, the nanoparticles (NP), particularly when embedded at low mass loads of 0.1%, significantly elevated the hydrophilicity of the polymer and also induced particular changes in polymer stiffness in the vicinity of the nanoparticles probed by AFM. In this case, very pronounced effects on pre-endothelialization were discovered, which was up to three times higher than in the unmodified TPU [12]. Another more frequently addressed effect in nanocomposites is the release of metal ions and their impact on the adhesion of cells [9, 13]. For example, iron ions are key to biological functions of erythropoiesis [14] and wound healing [15], which are all related to proteins.

In this context, the embedding of nanoparticles into polymers has been frequently studied and these nanocomposites are believed to serve as a reservoir for the release of metal ions [10]. Furthermore, the combination of laser-generated Ag nanoparticles with Mg, Zn, and Cu in TPU has been systematically investigated [11]. A broader therapeutic window, in which the materials were both toxic to bacteria and nontoxic to mammalian cells, was found. Another important ion-releasing additive in nanocomposites is iron nanoparticles. This is attributed to the fact that iron is an important biochemical factor, relevant to the structure of proteins and the metabolism of cells [16]. Recent studies revealed the effects of the molar concentration of Fe on the cell attachment and proliferation in Fe-phosphate glass fibres [17]. In another study, the influence of iron nanoparticles embedded into alginate tubes generated by 3D biofabrication was analyzed. Here, the embedding of low mass loads of Fe NPs (<0.1%) generated by *in situ* laser ablation in alginate solution had a pronounced effect on cellular activity, which is believed to be correlated with the release of the iron ions [4]. Zhao *et al* [18] focused on the adsorption of bovine serum albumin (BSA) on imprinted alginate/polyacrylamide hydrogel films, while Angar *et al* [19] examined the adsorption-desorption mechanism of BSA on hydrogels. These studies showed that protein adsorption on the surface plays a key role as an initial step for the interaction of cells with synthetic materials, often directly correlated with cellular adsorption [20, 21]. On a biomaterial scaffold, protein adsorption on the supramolecular level was proposed to affect the vascularization via interacting with typical integrins expressed by cells [22]. Further, the adsorption of cellular proteins like collagen on catheters was reported to be a promising strategy for vascular regeneration [23]. Thus, protein adsorption may be an initial indicator of cytocompatibility and may be used as biological readout to predict the cellular response of biomaterials.

Regarding the mechanism of metal ion release, Hahn *et al* investigated the Ag and Cu ion release kinetics from silicone composites generated by laser ablation in liquids [24, 25]. Wilke *et al* studied Zn ion release from microgel-modified fibers and found elevated Zn release at higher ZnO nanoparticle loadings in microfibers [26]. So far, the mechanism of diffusion-based release and multi-element release has already been considered; however, the effects of oxide solubility and the polymer matrix on Fe ion release have not been frequently

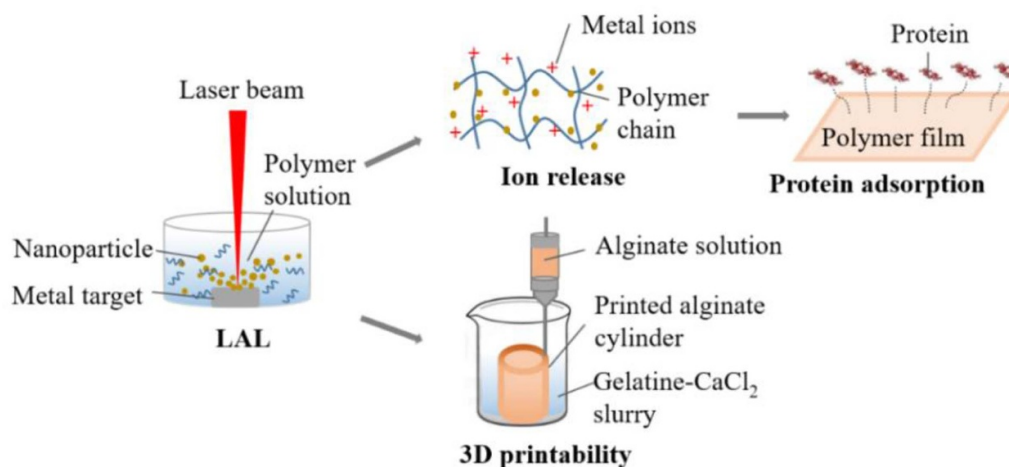


**Figure 1.** Procedure of the fabrication method, ion release kinetics from obtained nanoparticles embedded in alginate and TPU polymer matrix and 3D printability of alginate composites. Laser ablation in polymer solutions leads to *in situ* generation of nanoparticle-polymer composites. The special ion release and printability are promising for tissue engineering applications.

considered. Moreover, little is known about the inter-relation between protein adsorption and ion release in alginate nanoparticle polymer composites.

In the present study, nanoparticle-TPU or -alginate composites (nanocomposites) were prepared by laser ablation in liquids (LAL) [7, 27]. The detailed ion release kinetics, protein adsorption capacity, and the printability of alginate hydrogel were investigated (figure 1). These readouts are further correlated with the chemical (hydrophilicity, molecular structure) and physical properties (stiffness, swelling rate) of the composites. In detail, the following experiments were conducted: The size distributions of the generated nanoparticles in different polymer solutions were investigated. Further, the physicochemical properties, such as the surface charge and the wettability of the composites were determined. Meanwhile, the swelling ratios and porosities of alginate hydrogel composites were examined. We tested the dependence of the release of bioactive Fe ions from nanocomposites on the mass loading of Fe nanoparticles, choosing Zn and Cu nanoparticles in alginate as controls. Consecutively, the BSA adsorption capacity was tested as an initial indicator for the evaluation of the biocompatibility. In this context, we elucidate to what extent the affinity of BSA to the nanocomposite is correlated with the loading of the nanoparticles and the composition of the composite biomaterials. This study was finalized by verifying 3D printability of the nanoparticle-loaded alginate gels.

## 2. Materials and methods

### 2.1. Generation of nanoparticle composites via laser ablation

Alginate solutions were prepared by dissolving 1.5% m/v sodium alginate powder (Sigma, St. Louis, MO, USA) in deionized water. Thermoplastic polyurethane (TPU, Elastogran 1190 A) was kindly provided by BASF company, Germany. Tetrahydrofuran (THF, purity >99.9%; Sigma Aldrich) was used to dissolve TPU with a final polymer concentration

of 1 wt%. The polymer viscosity was measured with the instrument of Microviscometer (Lovis 2000 M, Anton Paar). The generation of metal (Au, Fe, Cu and Zn) nanoparticles was carried out by pulsed laser ablation of metal sheets in the polymer solutions using an Nd:YAG picosecond laser system (Atlantic, Ekspla) at its fundamental wavelength of 1064 nm. The Au (thickness 0.5 mm, Allgemeine Gold- and Silberscheideanstalt AG) and Fe (thickness 0.25 mm, Sigma-Aldrich) targets were of 99.99% purity, while Zn (Good fellow, thickness 0.1 mm) and Cu (Good fellow, thickness 0.5 mm) were of 99.95% purity. The pulsed laser beam was focused into a PTFE batch chamber, which contained the bulk metal target foil and a volume of 30 ml of the polymer solution. The pulse repetition rate was 100 kHz. During the ablation process, the liquid was stirred with a Teflon turbine driven by a motor. The constant flow ensured that already ablated material was transported away from the laser beam. The control samples of solutions of alginate and TPU were laser-processed in the absence of an ablation target. The nanoparticle concentration of the composites was determined by the weight difference of the ablation targets before and after laser ablation on an analytical balance (PESA Waagen, Switzerland). All the error bars in this work were from triplicated samples.

### 2.2. Characterization of composites

Transmission electron microscopy (TEM; Zeiss EM 910, 120 kV acceleration voltage) was employed to analyze the dispersions of colloidal, polymer-coated nanoparticles. A volume of 5–10  $\mu$ l of each solution was dropped on carbon-coated Cu grids. Subsequently, samples were dried in air at room temperature before placing them into the microscope. The statistical analysis of the particle size was carried out using the ImageJ software. To determine the number-weighted particle size distributions, primary particle diameters of at least 400 nanoparticles per sample were counted for statistical analysis. The data was plotted into number-weighted size histograms and fitted using a log-normal function to obtain the average

particle size. The polydispersity index (PDI) was calculated from the following equations [28]:

$$PDI = \frac{Var(x)}{x_c^2} \quad (1)$$

$$Var(x) = e^{2\ln(x_c) + w^2} (e^{w^2} - 1) \quad (2)$$

where  $x_c$  represents the average particle diameter and  $w^2$  is the standard deviation. To verify potential degradation or damage of the alginate monomer by laser ablation, we examined dry samples of alginate prior to and after laser irradiation via Fourier-transform infrared spectroscopy (FTIR, FT/IR-430, Jasco).

A Leica TCS SP8 epifluorescence confocal microscope connected to Leica LAS AF 3 software was used to investigate the 3D distribution of nanoparticles in TPU and gelled alginate composites via dark-field imaging. For Au nanoparticle composites, the excitation wavelength was 532 nm, and the emission wavelength was in the range of 534–590 nm. In the case of Fe, the excitation wavelength was at 470 nm and 532 nm while the emission wavelength in the range of 472–528 nm and 538–600 nm [4]. The obtained confocal microscopy images were processed with ImageJ software.

### 2.3. Swelling ratios and porosity of nanoparticle-alginate composites

To analyze the swelling ratios of the samples, the alginate and its composites were cross-linked with calcium chloride ( $\text{CaCl}_2$ , AppliChem). Briefly, 500  $\mu\text{l}$  of 25  $\text{mg ml}^{-1}$   $\text{CaCl}_2$  were cast into a 24-well plate (Eppendorf AG, Germany) and frozen at  $-20^\circ\text{C}$ . 500  $\mu\text{l}$  of 1.5% m/v alginate solution (pure alginate, nanoparticles- alginate) were added on top of this base layer. For complete gelation, the solutions were kept at room temperature for 30 min. The swelling ratio (S) of different samples was calculated using the following equation (3) [29]:

$$S = \frac{w_t - w_0}{w_0} \quad (3)$$

where  $w_0$  and  $w_t$  are the dry and wet weight, respectively. Here, the dry and wet weights were analyzed by analytical balance.

The porosity ( $P$ ) of the prepared discs of alginate composites was determined using a reported method [30]. Briefly, the discs were immersed in ethanol (Fisher Scientific, UK), a solvent that easily penetrates the pores without causing shrinkage or swelling [30], as displacement liquid until the discs were saturated. The samples were weighed before and after the immersion in alcohol. The porosity was calculated using equation (4):

$$P = \frac{w_1 - w_2}{\rho V_1} \quad (4)$$

where  $w_1$  and  $w_2$  indicate the weight of discs before and after immersion in ethanol, respectively.  $V_1$  is the volume before immersion in ethanol;  $\rho$  is the density of the alcohol.

### 2.4. Surface zeta potential of nanoparticles-TPU composites films

To obtain suitable films for measuring the surface zeta potential (streaming potential) of TPU composites, a TPU composite solution was cast into a glass petri dish. After drying, circular samples with 14 mm diameter and 0.2 mm of thickness were obtained by punching the thin films of the nanocomposites. All measurements were performed at pH values varied between 4.5 and 8.5, which were adjusted by adding 0.1 M KOH to the sample in volume increments of 0.02 ml. The streaming potential was measured by the device SurPASS Electrokinetic Analyzer (Anton Paar, USA). The surface zeta potential of the nanocomposites was calculated automatically by the software VisoLab, according to the given measured streaming current.

### 2.5. Contact angle of composites

Alginate and TPU nanocomposite films were prepared as described above. For labeling samples, alginate was abbreviated as Alg. The contact angles of the samples were measured by a Dataphysics OCA-15 instrument equipped with a video camera at room temperature by the captive bubble method. The contact angles of a captive air bubble and water were measured with a substrate fixed with composites films, facing downward in a square transparent glass vessel filled with deionized water. Once the air bubble was released from the J-shaped needle using a microsyringe beneath the glass substrate, images were captured within 30 s and contact angles were recorded by the software SCA20-F.

### 2.6. Ion release measurement

For the ion-release measurements, alginate discs and TPU nanocomposite films were placed in 50 ml tubes of polystyrene, which were previously cleaned by rinsing them in  $\text{HNO}_3$  (2%) and deionized water. Subsequently, 8 ml of 2 mM PIPES buffer, adjusted to pH 7.4, was added. The samples were incubated at room temperature. Samples of the supernatant (700  $\mu\text{l}$ ) were taken at different time points (0.15–100 h) without refilling fresh buffer medium, and nitric acid (1 vol%) was added to the samples for the stabilization of ions. The samples were stored at room temperature before measurement. The concentrations of metal ions in the sampled aliquots were analyzed with inductively coupled plasma mass spectrometry (ICP-MS, Perkin Elmer, Elan 6000) operating at 1000 W plasma power, 14  $\text{l min}^{-1}$  plasma gas flow, and 0.9  $\text{l min}^{-1}$  nebulizer gas flow. Prior to the analysis, the samples were diluted ten times with 1%  $\text{HNO}_3$  containing 10  $\mu\text{g l}^{-1}$  of yttrium (Y) and thulium (Tm) as internal standards. The washing time between measurements was set to 10 s with 1% suprapur  $\text{HNO}_3$  to avoid the contamination and memory effects. A series of 11 dilutions in the range of 0.1–100  $\mu\text{g l}^{-1}$  standard solution (ICP Multi-element-standard solution, Merck, Darmstadt, Germany Instrument) were used for the calibration. Metal ion concentrations ( $\mu\text{g l}^{-1}$ ) were calculated according to the corresponding calibration lines (correlation factor  $\geq 0.99$ ).

## 2.7. Protein adsorption of composites

The adsorption of proteins (BSA and collagen I obtained from Sigma Aldrich) on the alginate and TPU composites was carried out using a previously reported method [18, 31]. The surface water on alginate discs or TPU films was absorbed with clean filter paper to get the wet weight. Subsequently, samples were placed into 24 well plates containing 1 ml 0.5 mg ml<sup>-1</sup> BSA protein aqueous solution and collagen dissolved in 5 mM acetic acid, respectively, to evaluate the dynamic protein adsorption. The final pH was at 7.4. The whole protein adsorption process lasted for 1 h, and equilibrium adsorption capacity  $Q_e$  (mg g<sup>-1</sup>) of each sample was calculated according to the following equation (5) [18, 31]:

$$Q_e = (C_0 - C_e) V m^{-1} \quad (5)$$

where  $m$  (g) describes the mass of the wet hydrogel or the composites,  $V$  (ml) refers to the volume of the protein solution, and  $C_0$  (mg ml<sup>-1</sup>) and  $C_e$  (mg ml<sup>-1</sup>) are the protein concentrations of the initial solution and the supernatant solution at equilibrium, respectively. The protein concentrations of the supernatant solutions at equilibrium were determined by the Bradford method [32]. The calibration curves were built from the absorbance at 595 nm measured with a UV-vis spectrometer (Thermo Scientific) after mixing standard BSA protein with protein reagent for 2 min in 3 ml plastic cuvettes. The concentration of protein was plotted to determine the protein concentration in unknown samples, as shown in supplemental figure S1 (available online at [stacks.iop.org/NANO/31/405703/mmedia](https://stacks.iop.org/NANO/31/405703/mmedia)).

## 2.8. Demonstration of 3D printability

The printability of the alginate-nanoparticle composite was tested using a modular, compact 3D-bioprinter (SuperFill—Robo, Black Drop Biodrucker GmbH, Aachen, Germany). The system combines multiple 3D-printing modalities, such as drop-on-demand printing, microextrusion, and fused-filament-fabrication. The machine comprises three individually temperature controllable printer heads as well as a modular printing platform, which can be heated and cooled. The printing tests were conducted using a microextrusion printer head with a luer lock needle measuring 1.5 mm in diameter and 20 mm in length. A modified approach of the previously published submerged printing strategy was applied [33–35]. Briefly, a 10 ml glass beaker (Schott AG, Mainz, Germany) was filled with 10 ml of a crosslinker containing gelatin slurry. A stock of 10% (w/v) gelatin (gelatin type A, G2500, Sigma, St Louis, MO, USA) dissolved in 5% (w/v) calcium-chloride solution (CaCl<sub>2</sub>, AppliChem) was prepared. The gelatin was left to soak for 10 min at 24 °C until it formed a swollen slurry. The printing cartridge was carefully rinsed with ethanol and flushed with distilled water before it was loaded with either 1 ml of 1.5% (w/v) native alginate (i), iron-nanoparticle containing alginate (ii), or gold-nanoparticle containing alginate (iii). The beaker filled with the crosslinker-containing, swollen gelatin slurry was placed on the printing platform. The printing cartridge was loaded into the printer and the tip of the

needle was leveled to the bottom of the glass beaker. For the printing process the model of a cylinder was sliced into 0.2 mm thick layers (SuperFill—Slicer, Black Drop Biodrucker GmbH, Aachen, Germany). According to the previously created data set, the needle was moved layer by layer submerged in the gelatin-filled beaker. During the printing process uniform alginate strands were deposited under a pressure of 0.2 bar. In contact with the CaCl<sub>2</sub> containing gelatin, the printed alginate formed a solid gel after a short time. Following the printing process, the gelatin slurry was melted at 38 °C. After approximately 25 min the printed structures floated towards the surface and could be removed from the beaker with tweezers. Three specimens of each native, iron-, as well as gold-laden alginate were printed.

## 3. Results and discussions

### 3.1. Laser-based synthesis of nanoparticle-loaded alginate or TPU

A potential limitation of the *in situ* fabrication method of composites by lasers is the frequently discussed aspect of polymer degradation, in particular if femtosecond laser pulses are applied because of filamentation, and liquid ionisation, but also in case high intensity nanosecond pulses, which induce heating [27]. Here, picosecond laser pulse durations may provide a good compromise to minimize colloid excitation effects while minimizing target heating and thereby heat transfer from the target to the liquid. In order to verify potential degradation or damage of the alginate monomer by laser ablation, we examined blank alginate precursor solutions prior to and after laser irradiation via FTIR spectroscopy (figure S2), indicating that degradation was minimal.

During the ablation, experimental parameters such as the viscosity and the optical density of the liquid highly influenced the particle size and ablation efficiency [7, 8, 36]. With ns-laser, the Au NP productivity is obtained with a total value of 1100 ± 44 mg h<sup>-1</sup> [37]. Kohnsowski *et al* compared the nanoparticle productivities with ps-laser and ns-laser and found NP productivity related to the laser power [38]. With high power laser systems, the productivity of metal nanoparticles can reach 4 g h<sup>-1</sup> in water [39]. However, significantly reduced values are commonly found in organic solvents [36] and few works reported the NP productivity in polymer solutions [40].

In this study, productivity was reported for different mass concentrations of alginate and TPU in water and THF, respectively. A clear trend of reduced productivity with increasing polymer concentration was found, (figure 2, lower row). This was in accordance with the viscosity change of the studied polymer solutions, which was highly pronounced within the parameter matrix studied in this work (figure 2, upper row). For example, the viscosity of a 1.5% w/v alginate in deionized water is 18.8 mPa•s, while a 3.0% w/v stock solution had a seven times higher viscosity of 136.1 mPa•s. At 1.5% w/v alginate concentration, the NP productivity (53 mg Au h<sup>-1</sup>) was around two times higher than that in

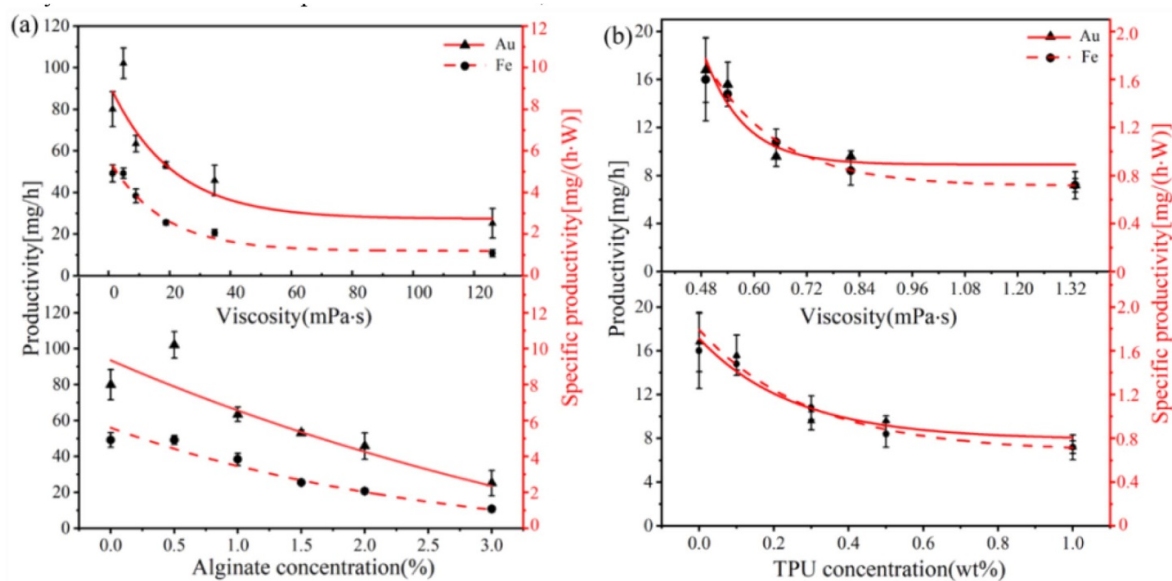


**Figure 2.** Influence of the concentration of alginate dissolved in water (a) and TPU in THF (b) on productivity during laser ablation using gold and iron targets.

3.0% w/v solution. And the highest specific nanoparticle productivity was calculated to be at  $5.5 \pm 0.4 \text{ mg (h}\cdot\text{W)}^{-1}$  for Au and  $2.1 \pm 0.2 \text{ mg (h}\cdot\text{W)}^{-1}$  for Fe. Nonetheless, the correlation between viscosity and productivity is not universal, as verified by a direct comparison between the alginate and TPU system. Although the viscosity of TPU/THF solution is  $1.33 \text{ mPa}\cdot\text{s}$  at the concentration of 1 wt%, the productivity of Au and Fe is around  $8 \text{ mg h}^{-1}$ , which is approximately 10 times lower than in an aqueous alginate system. In this context, the solvent (water vs. THF) seems to have a significantly more pronounced impact on productivity than the viscosity alone. The fact that nanoparticles synthesized in THF are larger (figure 3) and hence have higher absorption cross-sections might explain why the productivity in THF is lower compared to that in water, as Kalus *et al* [36] described because laser energy is absorbed or scattered by the colloid and can no longer be efficiently transferred to the target. In their work, Kalus *et al* also observed that the ascent speed of persistent gas bubbles in water is much faster and the bubbles' dwell time is shorter than in organic liquid, which also results in less shielding and consequently higher productivity in water. With regard to the different materials, Au mass productivity is usually higher than Fe in aqueous solution, a fact most likely attributed to different densities of Au and Fe. Considering this density effect, the ablated volume of Fe in our study is around 1.5 times higher than the volume of Au in this situation. Considering molar values, the number of ablated Fe atoms is around  $0.038 N_A$ , 2.2 times more than Au in 1.5% w/v alginate solution, whereas in 1 wt% TPU solution, this value is  $0.01 N_A$  for Fe, which is about 3.3 times more than ablated Au atoms.

The obtained colloids were characterized using TEM (figure 3). Metal nanoparticles revealed a uniform spherical morphology without the formation of aggregates, even though particle agglomeration can be frequently found [4]. The PDI describes the width of the particle size distribution. A narrow

size distribution has a PDI of 0.1–0.2, while polydisperse size distribution exceeds PDIs of 0.5 [28]. The PDI value of nanoparticles in alginate were 0.16 (Au) and 0.07 (Fe), while it was 0.7 (Au) and 0.56 (Fe) in TPU. Au nanoparticles synthesized in alginate solutions showed an average diameter of  $3.3 \pm 0.4 \text{ nm}$  (figure 3(a)), whereas Fe nanoparticles had an average diameter of  $8.0 \pm 0.1 \text{ nm}$  (figure 3(b)). In the case of TPU solutions, the obtained Au nanoparticles had average diameters of  $5.3 \pm 0.4 \text{ nm}$  (figure 3(c)), while the average size of Fe nanoparticles was  $12 \pm 2.9 \text{ nm}$  (figure 3(d)). In previous studies on the synthesis of Au nanoparticles in alginate using chemical reduction, the obtained particles were  $5 \pm 2 \text{ nm}$  in diameter [41]. For TPU, values in the range of 5–20 nm were reported [42]. The smaller particle size of Au compared to Fe may result from the laser ablation process. As stated in 3.1, more ablated Fe atoms may have facilitated the particle growth before it was quenched by the stabilizing polymer chains [43]. Furthermore, stronger interactions between the polymer chains and the gold nanoparticles are conceivable in contrast to iron, which could induce a more efficient size quenching.

Embedding metal nanoparticles into a polymer matrix may alter the roughness of the surface [23] and change the physicochemical properties [12], which may in turn influence protein interaction and cellular proliferation. Therefore, it is necessary to investigate the distribution of nanoparticles in polymers, as shown in figure 4. Laser scanning confocal microscopy (LSCM) is not only a powerful tool to investigate cells, but it may also be used as a high-throughput technique for examining nanoparticle-polymer composites [44], and investigating metallic nanoparticles [4, 45–47]. Confocal microscopy is very sensitive to the particle's geometry and polarizability while scattering patterns of metal nanoparticles are acquired. Due to the surface plasmon resonance (SPR) enhanced scattering, confocal microscopy can be used for the quantitative visualization of Au nanoparticles [4, 46]. Furthermore, single

spots could also be observed in the polymer. Klein *et al* [46] found that LSCM had a size detection limit of 60 nm for gold nanoparticles. It is well-known that azimuthally and radially polarized doughnut modes render different patterns: the signal of particles smaller than the resolution will be observed either as a ring or a spot with a weak surrounding ring of contrast, as proved by Züchner *et al* [45].

To verify the nanoparticle distribution in the whole volume of this thin polymer film, the composites were rotated in the *z*-axis to acquire 'living mode' images. During the laser ablation of a metal target in a polymer solution, the generated nanoparticles are immobilized by macromolecules and embedded into the polymers *in situ*. The 3D images confirmed this point (figures 4(c)–(f)). The results showed that most nanoparticles were homogeneously distributed in alginate and TPU. However, slight particle agglomeration was also found, which is in agreement with previous findings [4].

### 3.2. Surface zeta potential, swelling ratio, wettability and porosity of nanoparticles-polymer composites

As TPU composites are non-soluble in water, it is easy to study them under the flowing solutions with varied pH. Corresponding studies with alginate were not possible under these experimental conditions as the alginate gels exhibited a pH-dependent disintegration. Figure 5 depicts the surface zeta potential of TPU, Fe (0.09 wt%) or Au (0.17 wt%) TPU composite films as a function of pH. The surface charges of films result from bound dissociable groups or adsorbed charge carriers from the environment [48]. In general, the isoelectric point (IEP) of materials indicates their pH value of surface charge compensation and application potentials, e.g. cellular adhesion [49]. The TPU control showed positive surface zeta potentials in the pH range of 4.5–8.2 with an IEP at pH 8.2. In particular, at pH 7.4, TPU was positively charged (23 mV), which confirmed the experiments of Yu *et al* who demonstrated the zeta potential of TPU was 23 mV at pH 7.4 [5]. In contrast, the surface zeta potential for Fe- and Au-TPU was consistently negative at pH above 4.6. Furthermore, films with nanoparticles were negatively charged between –55 mV and –58 mV, as previously reported for TPU modified with Pt and Au nanoparticles [12]. Laser-generated noble metal nanoparticles are usually negatively charged [28], which seems to affect the surface of TPU.

To gain insight into the wettability of alginate and TPU nanocomposites, contact angle measurements by the captive bubble method were carried out. An air bubble was attached to the surface of samples as shown in the insert figures 6(a), (b). The contact angle measured using the captive bubble method is between the air bubble and surface, i.e.  $\theta_{\text{air}}$ , using the Laplace-Young fit. The water contact angle should be recalculated as  $180^\circ - \theta_{\text{air}}$ , and a low water contact angle indicates a more hydrophilic material. The results are depicted in figure 6. The surface of pure alginate and the nanocomposites showed an extremely high degree of hydrophilicity. The contact angle of pure alginate ( $17^\circ$ ) was reduced to  $7^\circ - 14^\circ$  in the presence of nanoparticles, indicating a slight increase in wettability. TPU and its composites were hydrophilic as well but

with a higher contact angle of approximately  $43^\circ - 60^\circ$ , which was in good agreement with previously reported results [12]. The contact angles were approximately  $60^\circ$  for pure TPU and  $43^\circ$  for Fe-TPU composites, indicating that Au and Fe nanoparticles improved the wettability of TPU. The contact angles of different nanoparticle loadings showed no significant differences (figure S3), probably attributed to the low differences in mass loads used here. These results were in accordance with other findings, where a more hydrophilic surface was obtained through embedding Pt or Au nanoparticles into TPU [12], or surface modification [50]. The observed change of the wettability proved that the incorporated nanoparticles altered the surface properties of the polymers. This finding is in good agreement with the zeta potential measurements, where particles embedded in TPU were shown to reverse the charge and increased the overall net charge of the composites by a factor of  $>2$ .

Swelling experiments were carried out in distilled water at room temperature and the evaluation of the porosity was performed for alginate composites by using ethanol (figure 7). The TPU-based nanocomposites were without macrospores. SEM images (figure S4) also confirmed that the native polymer is not porous and the NPs have no impact on porosity. The porous nature of the alginate can be helpful to absorb proteins and transport ions [30]. The swelling ratio analysis revealed that pure alginate featured a swelling of 10%. The embedding of AuNPs induced a steep increase of the swelling ratio up to an Au mass load of 0.1 wt%, while saturation was observed for higher mass loads (figure 7(b)). Embedding of Fe nanoparticles into alginate, on the other hand, leads to a significantly higher swelling up to 50% at a mass load of 0.7 wt%, though the total slope of the curve was lower than in the case of gold. Furthermore, a pronounced decrease in the swelling ratio was discovered for even higher Fe mass loads, which could not be observed in the case of Au. Note that the mass of nanoparticles in the 200–5000 ppm range, negligible in contrast to the weight of the alginate. The fact that an increasing amount of nanoparticles enhanced the swellability of hydrogel composites is in accordance with previous reports [51, 52]. This could be attributed to the fact that embedded nanoparticles may have caused the enlargement of alginate hydrogel networks [52], which enhances swelling capability. The pronounced difference between the swelling rates for gold and iron could be that iron, due to its lower density, would fill a higher volume of the gel at equal mass dose. In other words, iron-loaded gels contain a higher number of particles at the same mass load. Additionally, the Fe nanoparticles were reported to possess a significantly higher diameter in comparison to their Au analogs. Another interesting phenomenon is the shrinkage of the gel network at higher iron loads, which could not be observed for gold. This could be due to the fact that iron nanoparticles are soluble and release iron ions. At high iron mass loading, these ions could exceed a critical concentration where they interact with the alginate chains and induce further polymerization of the chains. This correlation will be discussed in more detail in conjunction with ion release studies. With regard to the polymers' porosities in figure 7(c), it was found that the porosities of pure alginate and

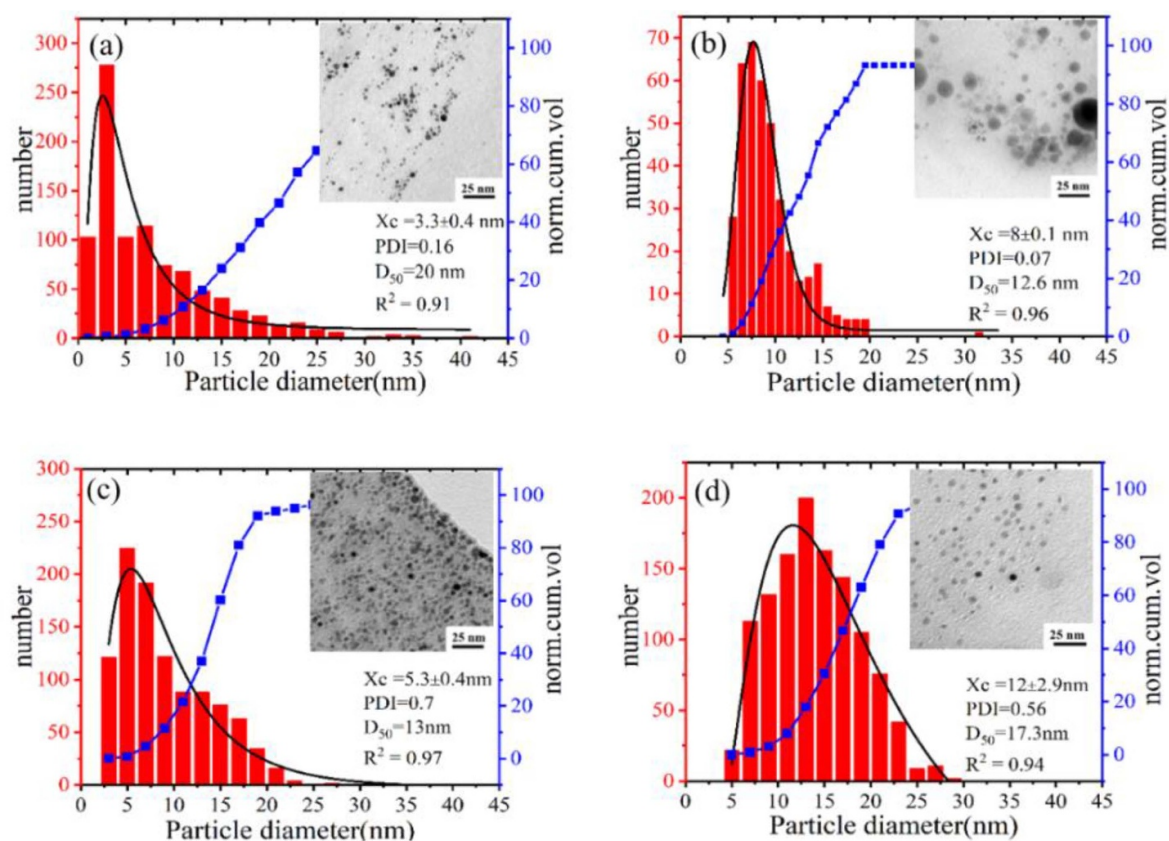


**Figure 3.** Particle size distributions and representative TEM images of nanoparticles generated by the laser ablation of metal plates in polymer solutions. The images show alginate filled with Au nanoparticles (0.043 wt.%) (a), alginate filled with Fe nanoparticles (0.03 wt.%) (b), TPU embedding with Au nanoparticles (0.069 wt.%) (c) and TPU embedding with Fe nanoparticles (0.048 wt.%) (d). Parameters of the log-normal fitting and the calculated PDI are given in the diagrams.

that of composite did not show any significant variations, both for embedding with Au or Fe nanoparticles up to mass loads of 0.9 wt%, respectively. All samples showed porosities in the range of 17% – 23%.

### 3.3. Ion release

Figures 8 and 9 illustrated the time-dependent Fe ion release from Fe-loaded alginate and TPU nanocomposites, respectively. The general trend of these curves was similar to other metal ion releasing profiles from laser-generated nanoparticle polymer composites, which followed the pseudo first-order equation [4, 11]. The accumulated ion release from Fe nanoparticle composites was obviously higher than the unloaded controls (figures 8(a) and 9(a)). The release of ions from pure alginate and pure TPU was probably induced by Fe impurities. After an initial increase within the first 10 h, the release profiles entered a plateau. Overall, the amount of released Fe ions from TPU nanocomposites was lower compared to alginate nanocomposites, which may result from a smaller Fe nanoparticle size in alginate and the porous hydrophilic gel structure, which eases ion transport via diffusion. Comparable release kinetics of Fe ions were also found for other nanocomposites in literature [9].

The obtained absolute Fe ion concentration in the case of Fe-TPU composites increased with the nanoparticle loading

(figures 9(a), (c)). On the other hand, the ion release in percent was found to decrease with increasing nanoparticle loads (figures 9(b), (d)). This behavior is in accordance with previous findings [9] and expectations, as a higher total release of ions is expected at higher particle loads. On the other hand, a diffusion-driven mechanism would slow down release in case of higher total ion concentrations in the medium, reducing the relative release under static experimental conditions. Irrespective of the expectations, the highest total amount of Fe ions was released from the alginate samples with lower nanoparticle loadings, such as 0.05 wt% and 0.1 wt% (figure 8(a)). Furthermore, the absolute maximum Fe ion concentration clearly decreased with increasing load of nanoparticles embedded within the alginate matrix, even though high deviations between the individual samples were found (figure 8(c)). The normalized (to the total mass of loaded Fe) curves of released Fe ions showed a much more pronounced trend, indicating an exponential decrease of the relative ion release with nanoparticle mass load, which saturates below 10% for mass loads >0.5% (figures 8(b) and (d)).

These findings for the alginate-iron system are in contrast to findings on other releases systems previously described in the literature, where the total release always increased with nanoparticle loading. In contrast, we here find an optimum ion release at low NP loading and a lower total ion release at higher nanoparticle loading. In the following section we aim



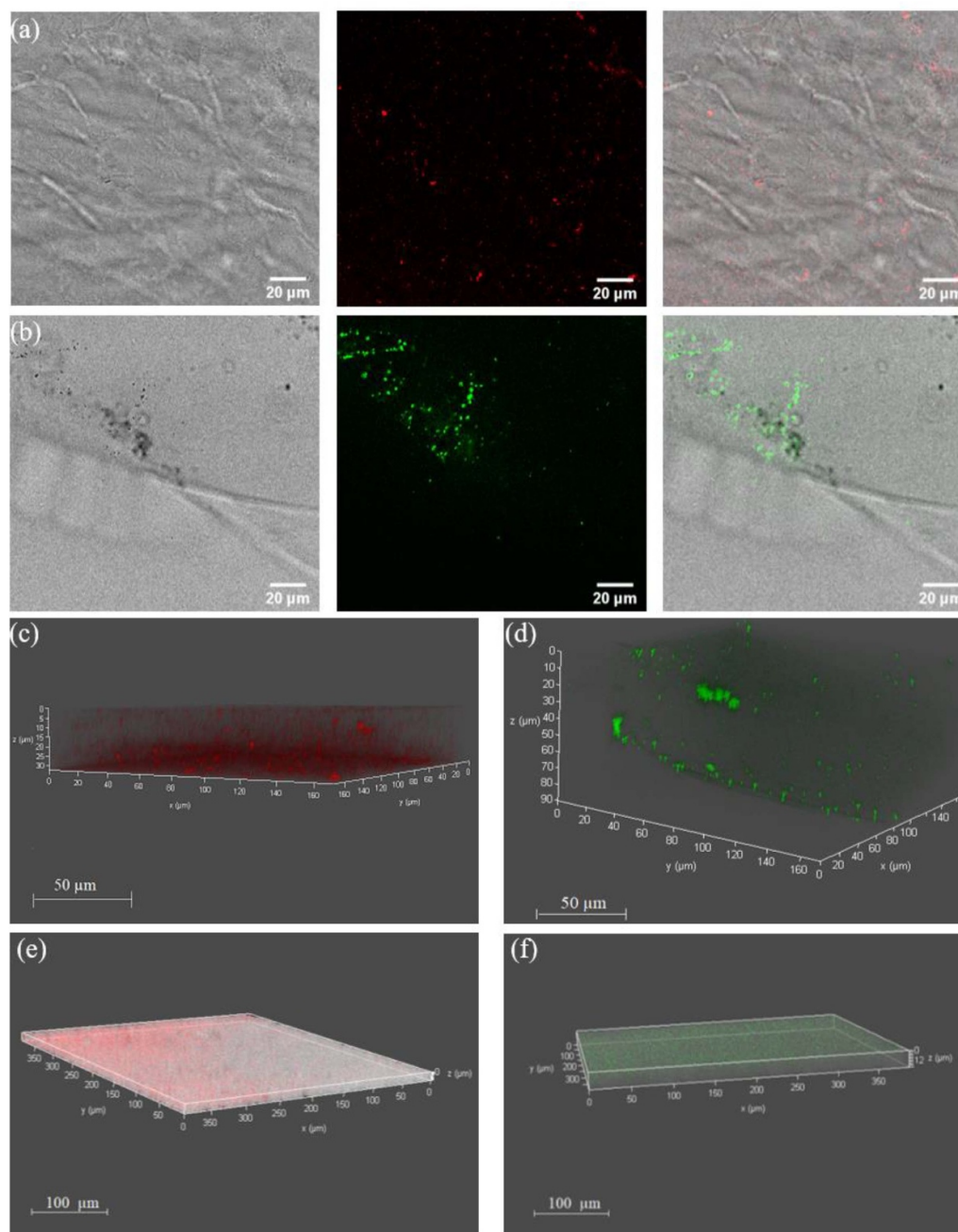


**Figure 4.** Laser scanning confocal microscopy images of grafted alginate and TPU filled with nanoparticles. Image reveals the particle distribution within the polymer matrix. Au nanoparticles (0.043 wt.%) in alginate (a), Fe nanoparticles (0.03 wt.%) in alginate (b) are shown. And left images represent the polymer matrix, middle means the nanoparticles and right is the overlays of nanoparticles and matrix. 3D images of grafted Au alginate composites (c), Fe–alginate composites (d), Au-TPU (0.069 wt.%) (e), and Fe-TPU (0.085 wt.%) (f) are shown.

to explain this phenomenon by discussing frequently reported effects like ion diffusion and element solubility, but also solubility of formed metal oxides as well as interactions between the ions and the polymer matrix, which are mostly neglected in literature.

Our initial hypothesis to explain this counter-intuitive phenomenon was that it may be related to a peculiarity of the alginate gel itself. To further investigate this correlation between the ion release and the loaded nanoparticle mass,

control experiments with Zn and Cu nanoparticles in alginate were conducted by following the identical experimental procedure (figure S5). The obtained results showed that the total concentration of released metal ions increased with the mass of Zn and Cu particles in alginate, while the total concentrations of Zn were much higher than for copper, which is in accordance with the more negative redox potential of Zn. The relative ion release slightly increased for Zn and decreased for Cu, however, the trends were far less pronounced than in

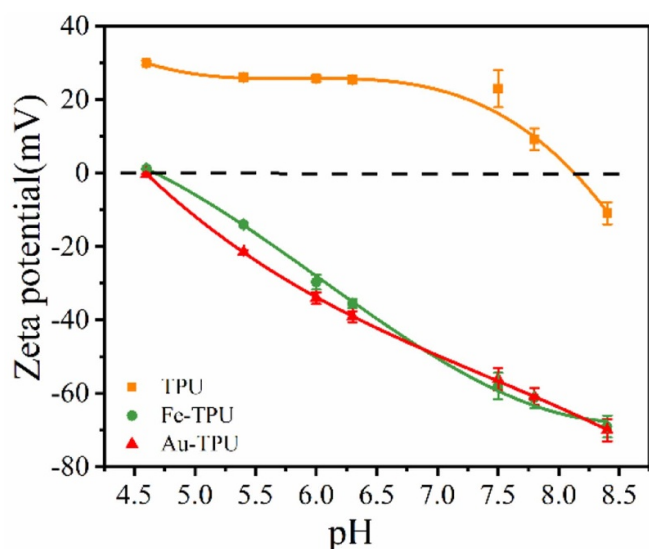


**Figure 5.** Surface zeta potentials of blank TPU, Fe-TPU (0.09 wt%), Au-TPU (0.17 wt%) derived from streaming potentials of TPU composite films at the variation with pH are shown. The plots were fitted with a polynomial function.

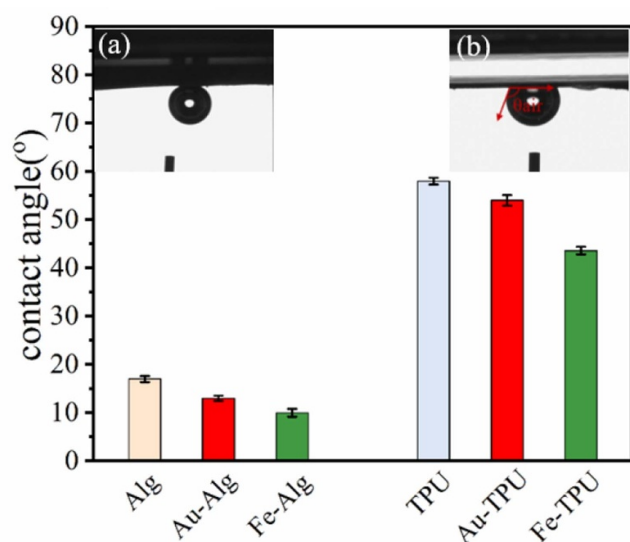


**Figure 6.** Contact angles of nanoparticles-alginate and nanoparticles-TPU composites are shown. Insert images showing how contact angle measurements are made using the captive bubble method: (a) alginate, Au (0.05 wt%), Fe (0.05 wt%) alginate composites, (b) TPU, Au-TPU (0.17 wt%), Fe-TPU (0.09 wt%) composites.

the case of iron. Based on this we can conclude that the iron-alginate gel system seems to have special release properties, where higher concentrations of particles in the gel seem to inhibit the release of iron ions or particularly pronounced burst release occurs at low mass load.

Figure 10 illustrates the individual mechanistic steps involved in the release of ions for Fe compared with Zn. The release of ions from nanoparticle-loaded gels is initially influenced by the diffusion of the solvent into the composite followed by the diffusion of the solvated ions out of the gel. The

ions diffuse through channels that consist of the already existing pores of the network structure of the polymer or are migration paths of already released ions and corroded nanoparticles [53]. Diffusion clearly explains the shape of the release curves in all samples as depicted. The initial burst release is probably related to the initial high concentration gradient between the vicinity of the nanoparticle and the outside of the gel as well as the fact that nanoparticles situated close to the gel surface have shorter diffusion paths and therefore induce a faster release. After about 10 h, the release saturates because the concentration gradient, which is the driving force for diffusion, levels, as concentrations inside and outside of the gel reach a steady state under static release conditions. However, as the diffusion coefficients of solvated  $\text{Fe}^{2+}/\text{Fe}^{3+}$ ,  $\text{Zn}^{2+}$ , and  $\text{Cu}^{+}/\text{Cu}^{2+}$  ions are not significantly different (the literature values are listed in Table S1), diffusion cannot account for the peculiar behavior of the iron system, where higher absolute iron mass is released at low particle mass load. The ion release is further influenced by the dissolution of the embedded metal particles. The oxidation ability of metal can be estimated using the electrochemical standard potentials ( $E^\circ$ ).  $E^\circ$  for the oxidative formation of  $\text{Zn}^{2+}$ ,  $\text{Fe}^{2+}$ , and  $\text{Cu}^{2+}$  from the corresponding metals is  $-0.762$ ,  $-0.447$  and  $0.342$  V, respectively, while the strongest release is expected for the most negative standard redox potential. Based on this we would expect a trend for the highest release rate and final ion concentration  $\text{Zn} > \text{Fe} > \text{Cu}$ . This trend can be clearly confirmed for higher particle mass loads. For example, at the 1.2 wt% loading of Zn and Cu, and 0.5 wt% of Fe, this trend can be observed as the resulting total ion concentration of Zn, Fe, and Cu was  $550$ ,  $300$ , and  $110 \mu\text{g l}^{-1}$  (figures 8(a) and S5(a)). However, the trend is significantly different at lower loads. For example, at 0.3 wt%, the total released mass of iron ions is 4–5 times higher. These findings cannot be explained by the redox potential of the corresponding metal nanoparticles.

Next to the direct oxidation of the pure metals in an aqueous medium, it is highly likely that the iron nanoparticles, laser-fabricated in aqueous medium, are at least partially oxidized. Using picosecond lasers, oxides are frequently obtained by the ablation of elemental targets in liquids, such as ZnO, CuO, FeO,  $\text{Fe}_3\text{O}_4$  [54]. The formation of possible  $\text{Fe}_3\text{C}$  species can also not be excluded in case ablation is conducted in organic solvents. In addition, it is known that laser ablation of ignoble metals in aqueous solution may lead to suboxide nanoparticles, or elemental core - oxide shell nanoparticles [64]. Based on the Pourbaix diagram in aqueous solution at 298 K and pH 7.4, oxides like ZnO,  $\text{Cu}_2\text{O}$ , CuO, FeO,  $\text{Fe}_2\text{O}_3$  and  $\text{Fe}_3\text{O}_4$  are likely to form. This shows that in case of iron, a number of different oxides could be formed. However, there are some indications in literature that FeO may be the predominant oxide under these conditions [55]. During the particle dissolution reaction in water, these oxides will initially form hydroxides that can dissolve to form metal ions. As a consequence, the solubility of these oxides may be an important contributing factor to the ion release mechanism [56]. For metal oxides, the following reactions occurred in water at pH 7.5, as Mudunkotuwa described for ZnO NPs [56]. Thereto we compared the solubility product constants  $K_{\text{sp}}$  of Zn, Cu and

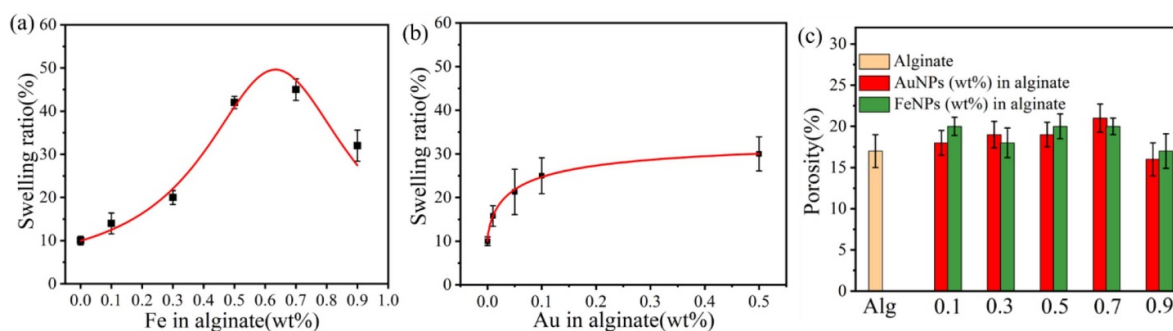


**Figure 7.** Swelling behavior of alginate with different amounts of Fe nanoparticles (a) and Au nanoparticles (b). Porosity evaluation of different loadings of Au and Fe nanoparticles in alginate (c).

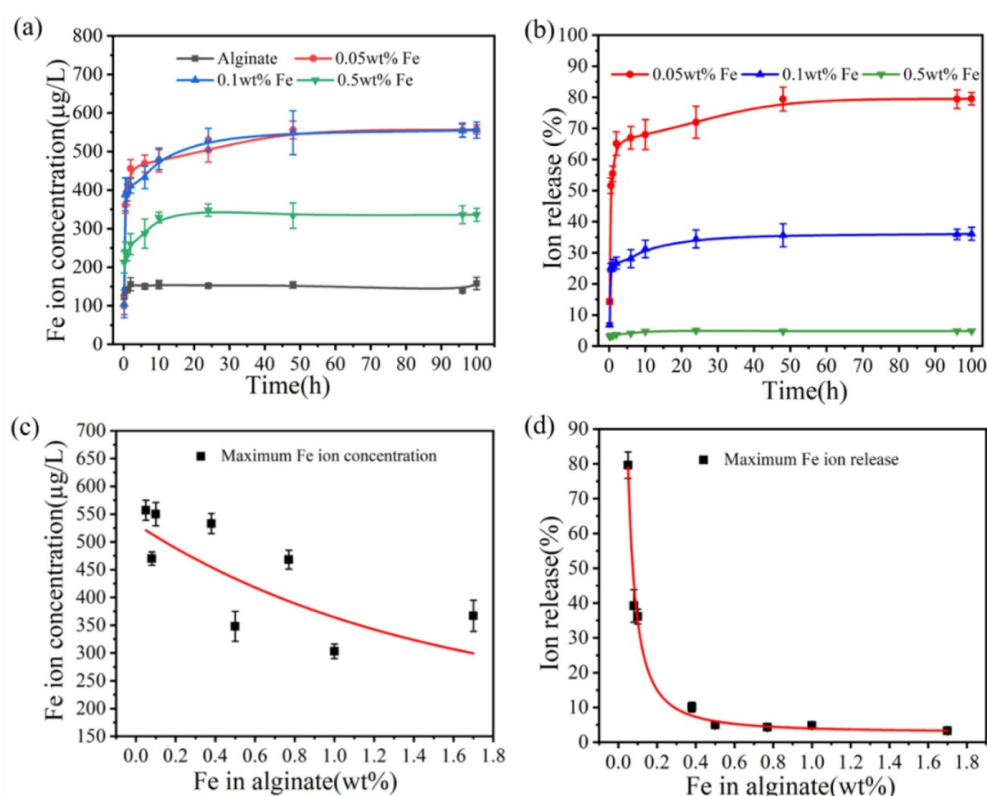
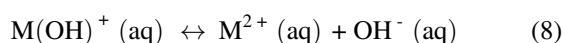
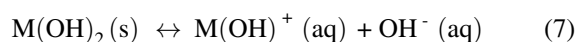


**Figure 8.** Long-term Fe ion release kinetics in the air-saturated physiological buffer: (a) released Fe ion concentration of Fe-alginate composites, (b) released mass percent of different amounts of Fe nanoparticles in alginate, (c) the maximum absolute Fe ion release and (d) the corresponding ion release percent of Fe-alginate composites.

Fe hydroxides (table S2).



The values clearly reveal that the  $K_{\text{sp}}$  value of  $\text{FeO}/\text{Fe}(\text{OH})_2$  is the highest followed by  $\text{ZnO}/\text{Zn}(\text{OH})_2$ , which is considerably higher than  $\text{CuO}/\text{Cu}(\text{OH})_2$ . The solubility constant for

the system  $\text{Fe}_3\text{O}_4/\text{Fe}(\text{OH})_3$  cannot be directly compared to the others due to deviating reaction stoichiometry. Based on this we can conclude that the higher solubility of the iron oxides may be a contributing factor to a stronger release of iron ions, however, it does not explain the peculiar particle mass load dependency of the release kinetics.

There to, one final aspect which needs to be considered concerns the interactions of the metal ions with the alginate matrix. The order of binding affinity of ions for alginate was:  $\text{Fe}^{2+} > \text{Fe}^{3+} > \text{Cu}^{2+} > \text{Zn}^{2+}$  [57, 58]. Jodra and Mijangos proposed an ion-exchange model between metals and calcium-gelated alginate gels [59]. According to this equi-

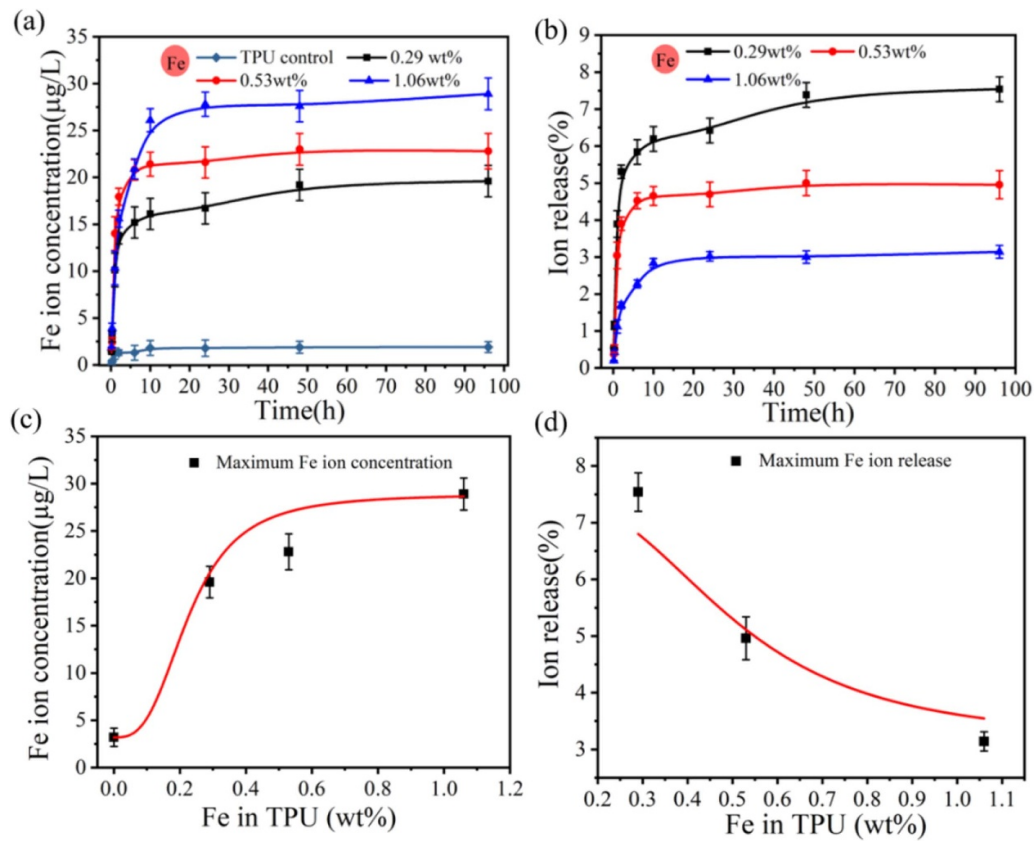


**Figure 9.** Long-term Fe ion release kinetics in physiological buffer: (a) released Fe ion concentration of Fe-TPU composites and the TPU control, (b) released mass percent of different amounts of Fe nanoparticles in TPU, (c) the maximum Fe ion release, (d) the corresponding ion release percent of Fe-TPU composites.

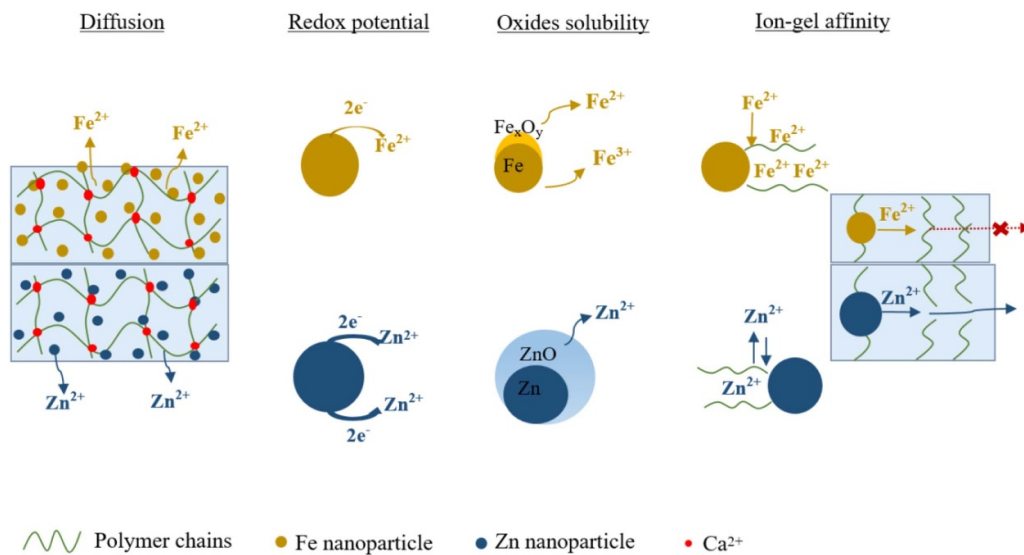
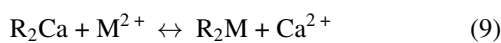


**Figure 10.** Schematic diagram of nanoparticle alginate composite specific Fe ion release mechanism compared with Zn.

librium model, the process was described by the next reaction and equation (10) [59]:



$$K_{Ca}^M = \frac{(q_M/C_M)}{(q_{Ca}/C_{Ca})} \quad (10)$$

where  $K$  is the corresponding equilibrium constant,  $q$  ( $\text{mol kg}^{-1}$ ) is the metal mass in alginate,  $C$  ( $\text{mol l}^{-1}$ ) is the metal concentration. Based on this we can conclude that the strong affinity of the iron ions for the alginate chains would shift the dissolution equilibrium of the FeO to the side of the soluble  $\text{Fe}^{2+}$ , while furthermore the solubility of the FeO is

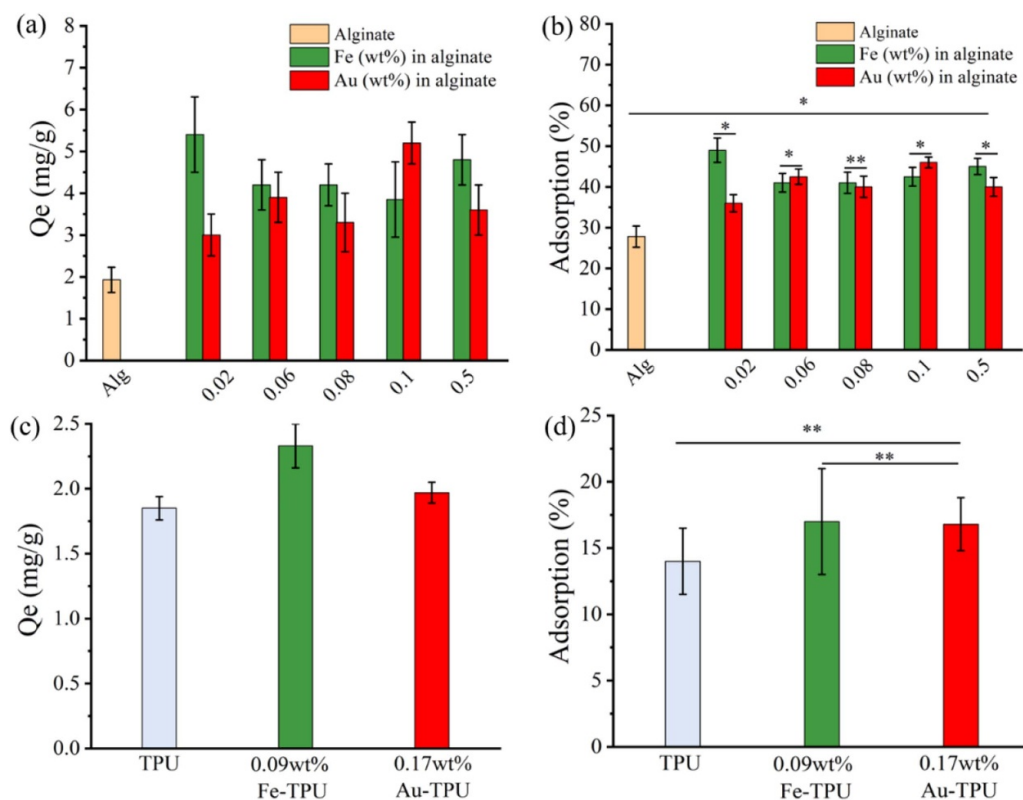
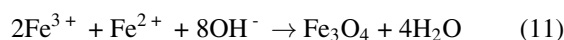


**Figure 11.** Protein adsorption on pure alginate, TPU, and corresponding composites as a function of nanoparticle concentration at pH 7.4 and room temperature: (a) and (b) protein adsorption on alginate and the composites, (c) and (d) protein adsorption on TPU and the composites. Statistical significance levels were evaluated with single factor analysis of variance (ANOVA) and significance levels were  $p < 0.05$  (\*) and  $p < 0.01$  (\*\*). (% refers to adsorbed protein vs. deployed protein.).

higher than that of CuO and ZnO. The combination of these two factors may account for the irregular burst release of iron ions at low loadings. However, why is the release inhibited at higher iron mass loads? In this context two factors could contribute. Firstly, high iron ion concentrations may favor the formation of low solubility oxides like  $\text{Fe}_3\text{O}_4$  according to reaction (11).



Furthermore, Fe ions have the highest affinity for alginate which may further influence the alginate network by inducing additional gelation processes and reducing pore diameters in the gel network. This assumption is backed by the measurements of the swelling rates, which tended to slightly decrease for iron nanoparticle loads exceeding 0.7 wt% (figure 7(a)). Hence, the higher ion concentration contributes to decreasing the porosity of alginate gels, which will inhibit the release at the higher Fe mass loads [60]. Considering the described factors, it is not the redox potential of the metals and diffusion of metal ions, but most likely the solubility of nano metal oxides and affinity of metal ions for alginate that lead to the special release behaviors of iron ions from iron-alginate nano-composite gels.

### 3.4. Protein adsorption of composites

The comparison of the protein adsorption capacity of Au- and Fe-alginate composites as well as of pure alginate is summarized in figures 11(a), (b). There is a clear trend revealing an elevated protein adsorption capacity compared to pure alginate ( $1.93 \pm 0.3 \text{ mg g}^{-1}$ ). Apparently, minute loadings of the composites with iron (0.02 wt%) have a very strong effect on protein adsorption, increasing the protein mass by a factor of 2.8 ( $5.4 \pm 0.9 \text{ mg BSA g}^{-1}$  composite). Interestingly, this steep increase in protein adsorption occurs in the same concentration regime where highly pronounced ion release is reported. This is in good accordance with cell culture experiments on similar systems where Bläser *et al* indicated that 0.01 wt% Fe-alginate gels strongly favor cell adhesion [4]. For higher Fe nanoparticle loads, there is a slight decrease in protein adsorption capacity, however, the values are still higher than the pure alginate control. For the case of Au-alginate composites, there is no steep increase of protein adsorption at low mass load but a constant increase with a local maximum at  $5.0 \pm 0.5 \text{ mg g}^{-1}$  at the concentration of 0.1 wt%. In another experimental approach, protein adsorption on nanoparticle-loaded TPU composites was studied at a constant nanoparticle mass load. As shown in figure 11(c), the adsorption of BSA slightly increased with embedding nanoparticles in TPU compared to the pure TPU films. The maximum  $Q_e$  was  $2.33 \pm 0.17 \text{ mg g}^{-1}$  for the

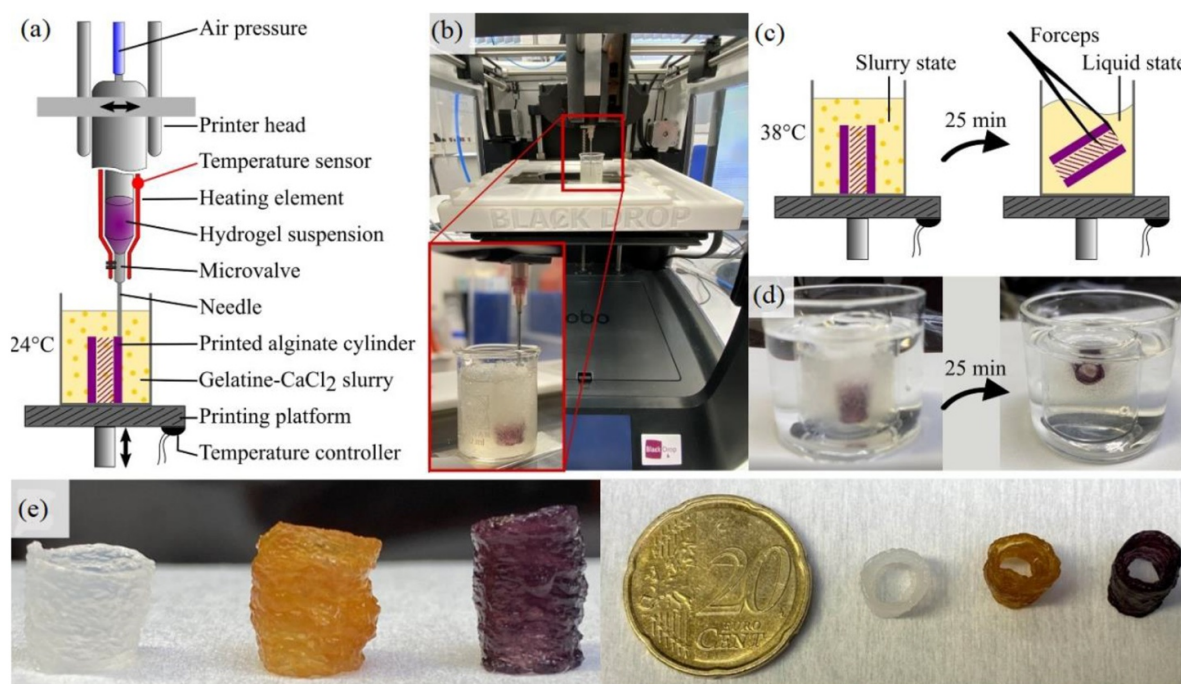


**Figure 12.** Submerged bioprinting of 3D-hydrogel scaffolds made of alginate composite bioinks. The printing process is illustrated schematically (a) as well as in overview and close-up images (b). To stabilize and crosslink the printed alginate constructs, the bioprinting process is conducted submerged in a gelatin- $\text{CaCl}_2$  slurry. After successful printing the slurry is heated up to  $38^\circ\text{C}$  to melt the gelatin and enable gentle removal of the printed object. The two slurry states (swollen and melted) are illustrated schematically (c) as well as with recorded images (d). Images of the bioprinted 3D-cylinders (e) are shown in side view (left) as well as in top view (right).

Fe-TPU composites. On the other hand, the type of embedded nanoparticles (Fe or Au) had no observable impact on protein adsorption. For further clarification and to rule out cross effects from different protein concentrations studied, the relative amount of adsorbed protein was plotted versus the nanoparticle loading in the composites (figures 11(b), (d)). Nanoparticle-alginate composites adsorbed more BSA than pure alginate, and the adsorption was approximately 1.7 times that of pure alginate. This phenomenon was also found in the collagen I protein adsorption as shown in figure S6. As a control, collagen I in contrast to BSA, is positively charged at pH 7.4 as indicated in the literature [61]. Our results also showed that the integration of minute amounts of nanoparticles has a universally beneficial effect on protein adsorption, both for albumin and collagen I. This seems to indicate that the net charge of the protein alone is not the dominant factor driving the adsorption process. The impact on TPU was less pronounced, as indicated by the adsorption rate of Fe-TPU composites at 17%, while the value was 14% for the TPU control.

The adsorption of proteins on a surface is a complex process, which is affected by the morphology, the ion-exchange, the surface charge, hydrogen bonds, van der Waals interaction and electrostatic interactions [20, 62]. The first step of protein adsorption is a fast direct-attachment to the surface, while the second step is slow and the thickness of the protein layer gradually increases with the increasing amount [20]. Generally, proteins preferred hydrophobic surfaces to hydrophilic ones. However, there is also evidence about protein adsorption on hydrophilic surfaces. In an aqueous environment, the available possibilities for hydrogen bonding involve

the residual amide molecules which form water-amide hydrogen bonds [62]. According to the experimental results, there is protein adherent on the alginate hydrophilic surface. However, we still cannot name alginate surface as ‘protein-adsorbing’ or ‘non-protein adsorbing’. The possible explanation could be that hydrophilic surface sites would attract proteins by electrostatic interactions. Moreover, the porous structure of alginate gels provides the channels for protein adsorption. Another important factor is the presence of Au and Fe nanoparticles, which can alter the morphology. Nanoparticles have a high affinity to amine and cysteine groups of proteins, especially for AuNPs. Additionally, the increasing ionic strength resulting from the Fe ion release was proved to favor the adsorption of larger amounts of protein [62]. Therefore, the hydrophobic or hydrophilic surface was not a significant parameter that contributed to the fact that much more protein was adsorbed on alginate hydrogels compared to TPU. But the porous structure of the alginate composites and the stronger release of ions play a prominent role in this situation. This demonstrates high application potential of composites as only minute amounts of NPs in the ppm range, significantly improve protein adsorption known to facilitate cell adhesion and growth.

### 3.5. 3D printing of scaffolds

Since nanoparticle addition triggers ion release as well as strongly enhances protein adsorption, the NP-laden polymers may be a widely applied in tissue engineering and 3D scaffold design. Hence, the question arises whether printability of the alginate-based composite materials is retained after the

addition of the nanoparticles. The printability of the alginate-nanoparticle composite and its potential applicability as bioink were tested following a novel 3D-bioprinting approach. Using a modular, compact 3D-bioprinter (SuperFill—Robo, Black Drop Biodrucker GmbH, Aachen, Germany) a modification of the previously published methods for FRESH or submerged bioprinting was applied [33–35, 63]. Briefly, a microextrusion bioprinting process was conducted submerged in calcium-chloride doped gelatin slurry (figures 12(a) and (b)). Defined strands of native, iron-, or gold-nanoparticle-laden alginate were printed to form hollow cylinders measuring 7 mm in diameter and up to 13 mm in height (figure 12(e)). The gelatin slurry did not only support the built-up mechanically but also provided the crosslinker to form a stable gel within seconds after printing. In order to remove the printed parts, the slurry was heated to 38 °C for 25 min (figures 12(c) and (d)).

The results of the printing test indicate that the integration of laser-generated metal nanocomposites does not hamper the process- and printability of alginate hydrogels. Instead, the composite was shown to be an ideal bioink for the submerged fabrication of versatile 3D constructs with relatively high strength that can support its self-weights during printing. And NPs homogeneously distributed in the 3D printing tubes. In figure 12(e) coloration of the mesoscopic 3D parts by the nanoparticles is clearly observable.

#### 4. Conclusion

In summary, this work demonstrates that laser ablation is a promising strategy to produce nanoparticle polymer (alginate hydrogel and thermoplastic polyurethane) composites with efficient productivity and printability for biological applications. As these biologically relevant nanocomposites are quite effective at low loadings far below 0.1 wt% (e.g. as low as 1000 ppm for Fe-alginate), laser ablation in liquid can be efficiently used for large scale production of these materials. According to our present productivity, this kind of composites with 0.1 wt% loading could reach 4 kg h<sup>-1</sup> and 2 kg h<sup>-1</sup> for Au and Fe composites, respectively. We identified laser-generated composites with small particle sizes while the particles were well-distributed in the polymer matrices. The embedding of nanoparticles was found to affect the physicochemical properties, mainly including wettability, surface charge, porosity and ion release kinetics. A higher release of Fe ions was detected at relatively lower loading mass of Fe nanoparticles, specifically in the alginate polymer. This peculiar behavior is probably attributed to the higher solubility of iron oxide in contrast to its Zn and Cu analog, as well as with the high affinity of the released Fe ions to the alginate network. In TPU, similar to the other polymer systems studies before in laser synthesis, like silicone and agarose, the ion-related effects were proportional to the nanoparticle loading. This polymer-specific behavior constitutes a finding highly relevant for the understanding of ion release processes from nanocomposites and could greatly improve the design of medically-relevant ion release systems where less is more and low loadings lead to a maximum impact. The ion release properties as well as

porosity of gels in turn led to the significantly enhanced BSA and collagen I protein adsorption on alginate surfaces. Overall, the results gain fundamental insights for future biomaterial design to control Fe ion release and the protein adsorption process, which is an important index to cellular response and biomedical devices, not limited to 3D printing. Based on these excellent properties, the presently prepared composites possess great potential for applications in tissue engineering and bioactive ion delivery, where a controlled release of metal ions could induce beneficial effects in the cellular response.

#### Acknowledgments

The authors thank the Imaging Center Essen (IMCES) (Institute for experimental immunology and imaging) for providing the confocal microscope and analyzing software. It is highly appreciated that Jurji Jakobi performed acquisition of the TEM images. Furthermore, we thank Dr Friedrich Waag for fruitful discussions as well as Dr Jacob Johny and Dr Carmen Streich for proofreading the manuscript. Yaya Li further acknowledges the China Scholarship Council for financial support.

#### ORCID iDs

Bernd Sures  <https://orcid.org/0000-0001-6865-6186>

Stephan Barcikowski  <https://orcid.org/0000-0002-9739-7272>

#### References

- [1] He X *et al* 2019 Rubidium-containing calcium alginate hydrogel for antibacterial and diabetic skin wound healing applications *ACS Biomater. Sci. Eng.* **5** 4726
- [2] Doderio A, Scarfi S, Pozzolini M, Vicini S, Alloisio M and Castellano M 2020 Alginate-based electrospun membranes containing ZnO nanoparticles as potential wound healing patches: biological, mechanical, and physicochemical characterization *ACS Appl. Mater. Interfaces* **12** 3371
- [3] Olate-Moya F, Arens L, Wilhelm M, Mateos-Timoneda M A, Engel E and Palza H 2020 Chondroinductive alginate-based hydrogels having graphene oxide for 3D printed scaffold fabrication *ACS Appl. Mater. Interfaces* **12** 4343
- [4] Blaeser A, Million N, Campos D F D, Gamrad L, Köpf M, Rehbock C, Nachev M, Sures B, Barcikowski S and Fischer H 2016 Laser-based in situ embedding of metal nanoparticles into bioextruded alginate hydrogel tubes enhances human endothelial cell adhesion *Nano Res.* **9** 3407
- [5] Yu D G, Lin W C, Lin C H, Yeh Y H and Yang M C 2007 Construction of antithrombogenic polyelectrolyte multilayer on thermoplastic polyurethane via layer-by-layer self-assembly technique *J. Biomed. Mater. Res. B* **83** 105
- [6] Wagener P, Brandes G, Schwenke A and Barcikowski S 2011 Impact of in situ polymer coating on particle dispersion into solid laser-generated nanocomposites *Phys. Chem. Chem. Phys.* **13** 5120
- [7] Zhang D and Gökce B 2017 Perspective of laser-prototyping nanoparticle-polymer composites *Appl. Surf. Sci.* **392** 991
- [8] Maurer E, Barcikowski S and Gökce B 2017 Process chain for the fabrication of nanoparticle polymer composites by laser ablation synthesis *Chem. Eng. Technol.* **40** 1535
- [9] Abou Neel E A, Ahmed I, Blaker J J, Bismarck A, Boccaccini A R, Lewis M P, Nazhat S N and Knowles J C

- 2005 Effect of iron on the surface, degradation and ion release properties of phosphate-based glass fibres *Acta Biomater.* **1** 553
- [10] GhavamiNejad A *et al* 2015 Mussel-inspired electrospun nanofibers functionalized with size-controlled silver nanoparticles for wound dressing application *ACS Appl. Mater. Interfaces* **7** 12176
- [11] Sowa-Söhle E N, Schwenke A, Wagener P, Weiss A, Wiegel H, Sajti C L, Haverich A, Barcikowski S and Loos A 2013 Antimicrobial efficacy, cytotoxicity, and ion release of mixed metal (Ag, Cu, Zn, Mg) nanoparticle polymer composite implant material *BioNanoMaterials* **14** 217
- [12] Hess C, Schwenke A, Wagener P, Franzka S, Laszlo Sajti C, Pflaum M, Wiegmann B, Haverich A and Barcikowski S 2014 Dose-dependent surface endothelialization and biocompatibility of polyurethane noble metal nanocomposites *J. Biomed. Mater. Res. A* **102** 1909
- [13] Jeong S H, Shin D Y, Kang I K, Song E H, Seong Y J, Park J U and Kim H E 2018 Effective wound healing by antibacterial and bioactive calcium-fluoride-containing composite hydrogel dressings prepared using in situ precipitation *ACS Biomater. Sci. Eng.* **4** 2380
- [14] Bouchnita A, Rocca A, Fanchon E, Koury M J, Moulis J M and Volpert V 2016 Multi-scale modelling of erythropoiesis and hemoglobin production *J. Inorg. Organomet. Polym. Mater.* **26** 1362
- [15] Williams S, Okolie C L, Deshmukh J, Hawco L, McNeil J, Nganou Assonkeng A C, Bennett C and Mkandawire M 2019 Magnetizing cellulose fibers with CoFe<sub>2</sub>O<sub>4</sub> nanoparticles for smart wound dressing for healing monitoring capability *ACS Appl. Bio Mater.* **2** 5653
- [16] Abbaspour N, Hurrell R and Kelishadi R 2014 Review on iron and its importance for human health *J. Res. Med. Sci.* **19** 164
- [17] Ahmed I, Collins C A, Lewis M P, Olsen I and Knowles J C 2004 Processing, characterisation and biocompatibility of iron-phosphate glass fibres for tissue engineering *Biomaterials* **25** 3223
- [18] Zhao K, Chen T, Lin B, Cui W, Kan B, Yang N, Zhou X, Zhang X and Wei J 2015 Adsorption and recognition of protein molecular imprinted calcium alginate/polyacrylamide hydrogel film with good regeneration performance and high toughness *React. Funct. Polym.* **87** 7
- [19] Angar N E and Aliouche D 2017 An enhanced immobilization of BSA biomolecule on anionic hydrogels: swelling and adsorption modeling *Chem. Pap.* **71** 1389
- [20] Nakanishi K, Sakiyama T and Imamura K 2001 On the adsorption of proteins on solid surfaces, a common but very complicated phenomenon *J. Biosci. Bioeng.* **91** 233
- [21] Yang H M, Teoh J Y, Yim G H, Park Y, Kim Y G, Kim J and Yoo D 2020 Label-free analysis of multivalent protein binding using bioresponsive nanogels and surface plasmon resonance (SPR) *ACS Appl. Mater. Interfaces* **12** 5413
- [22] Hasan A, Pattanayek S K and Pandey L M 2018 Effect of functional groups of self-assembled monolayers on protein adsorption and initial cell adhesion *ACS Biomater. Sci. Eng.* **4** 3224
- [23] Hsieh S C *et al* 2016 Prominent vascularization capacity of mesenchymal stem cells in collagen-gold nanocomposites *ACS Appl. Mater. Interfaces* **8** 28982
- [24] Hahn A, Brandes G, Wagener P and Barcikowski S 2011 Metal ion release kinetics from nanoparticle silicone composites *J. Control. Release* **154** 164
- [25] Hahn A, Gunther S, Wagener P and Barcikowski S 2011 Electrochemistry-controlled metal ion release from silicone elastomer nanocomposites through combination of different metal nanoparticles *J. Mater. Chem.* **21** 10287
- [26] Wilke P, Coger V, Nachev M, Schachschal S, Million N, Barcikowski S, Sures B, Reimers K, Vogt P M and Pich A 2015 Biocompatible microgel-modified electrospun fibers for zinc ion release *Polymer* **61** 163
- [27] Zhang D, Gokce B and Barcikowski S 2017 Laser synthesis and processing of colloids: fundamentals and applications *Chem. Rev.* **117** 3990
- [28] Streich C 2017 Laser-synthesized bioconjugated noble metal nanoparticles—rational design and efficacy against pathological protein aggregation *Doctoral thesis* Universität Duisburg-Essen
- [29] Lin N, Huang J, Chang P R, Feng L and Yu J 2011 Effect of polysaccharide nanocrystals on structure, properties, and drug release kinetics of alginate-based microspheres *Colloids Surf. B* **85** 270
- [30] Catanzano O *et al* 2018 Macroporous alginate foams crosslinked with strontium for bone tissue engineering *Carbohydr. Polym.* **202** 72
- [31] Bergaoui M, Aguir C, Khalfaoui M, Enciso E, Duclaux L, Reinert L and Fierro J L G 2017 New insights in the adsorption of bovine serum albumin onto carbon nanoparticles derived from organic resin: experimental and theoretical studies *Micropor. Mesopor. Mater.* **241** 418
- [32] Bradford M M 1976 A rapid and sensitive method for the quantitation of microgram quantities of protein utilizing the principle of protein-dye binding *Anal. Biochem.* **72** 248
- [33] Blaeser A, Duarte Campos D F, Puster U, Richtering W, Stevens M M and Fischer H 2016 Controlling shear stress in 3D bioprinting is a key factor to balance printing resolution and stem cell integrity *Adv. Healthcare Mater.* **5** 326
- [34] Duarte Campos D F, Blaeser A, Weber M, Jäkel J, Neuss S, Jahnen-Dechent W and Fischer H 2012 Three-dimensional printing of stem cell-laden hydrogels submerged in a hydrophobic high-density fluid *Biofabrication* **5** 015003
- [35] Blaeser A, Duarte Campos D F, Weber M, Neuss S, Theek B, Fischer H and Jahnen-Dechent W 2013 Biofabrication under fluorocarbon: a novel freeform fabrication technique to generate high aspect ratio tissue-engineered constructs *BioResearch Open Access* **2** 374
- [36] Kalus M R, Barsch N, Streubel R, Gokce E, Barcikowski S and Gökce B 2017 How persistent microbubbles shield nanoparticle productivity in laser synthesis of colloids—quantification of their volume, dwell dynamics, and gas composition *Phys. Chem. Chem. Phys.* **19** 7112
- [37] Kalus M R, Lanyumba R, Lorenzo-Parodi N, Jochmann M A, Kerpen K, Hagemann U, Schmidt T C, Barcikowski S and Gökce B 2019 Determining the role of redox-active materials during laser-induced water decomposition *Phys. Chem. Chem. Phys.* **21** 18636
- [38] Kohnsowski S, Seiser F, Wiederrecht J P, Reichenberger S, Vinnay T, Barcikowski S and Marzun G 2019 Effective size separation of laser-generated, surfactant-free nanoparticles by continuous centrifugation *Nanotechnology* **31** 095603
- [39] Streubel R, Bendt G and Gökce B 2016 Pilot-scale synthesis of metal nanoparticles by high-speed pulsed laser ablation in liquids *Nanotechnology* **27** 205602
- [40] Million N, Coger V, Wilke P, Rehbock C, Vogt P M, Pich A and Barcikowski S 2017 Water-based, surfactant-free cytocompatible nanoparticle-microgel-composite biomaterials—rational design by laser synthesis, processing into fiber pads and impact on cell proliferation *BioNanoMaterials* **18** 20170004
- [41] Saha S, Pal A, Kundu S, Basu S and Pal T 2010 Photochemical green synthesis of calcium-alginate-stabilized Ag and Au nanoparticles and their catalytic application to 4-nitrophenol reduction *Langmuir* **26** 2885
- [42] Lentz D M, Rhoades A M, Pyles R A, Haider K W, Angelone M S and Hedden R C 2011 Combinatorial study of a gold nanoparticle infusion process in a polymer film *J. Nanopart. Res.* **13** 4795



- [43] Letzel A *et al* 2019 Time and mechanism of nanoparticle functionalization by macromolecular ligands during pulsed laser ablation in liquids *Langmuir* **35** 3038
- [44] Zammarano M, Sung L P, Gilman J, McCarthy E, Kim Y S and Fox D M 2011 Revealing the interface in polymer nanocomposites *ACS Nano* **5** 3391
- [45] Züchner T, Failla A V, Hartschuh A and Meixner A J 2008 A novel approach to detect and characterize the scattering patterns of single Au nanoparticles using confocal microscopy *J. Microsc.* **229** 337
- [46] Klein S, Petersen S, Taylor U, Rath D and Barcikowski S 2010 Quantitative visualization of colloidal and intracellular gold nanoparticles by confocal microscopy *J. Biomed. Opt.* **15** 036015
- [47] Mugesh S, Arun R, Arunkumar K and Murugan M 2019 Synthesis of biogenic copper nanoparticles embedded in graphene oxide-chitosan composite and its anti-bacterial and cytotoxic activities *J. Nanosci. Nanotechnol.* **19** 2625
- [48] Schurz J, Erk G, Schempp W and Ribitsch V 1990 Zeta potential as an analytical tool for graft copolymers and for polymer surfaces *J. Macromol. Sci. A* **27** 1673
- [49] Cuddy M F, Poda A R and Brantley L N 2013 Determination of isoelectric points and the role of pH for common quartz crystal microbalance sensors *ACS Appl. Mater. Interfaces* **5** 3514
- [50] Chng S, Moloney M G and Wu L Y L 2018 Photochromic materials by postpolymerisation surface modification *ACS Omega* **3** 15554
- [51] Thomas V, Namdeo M, Murali Mohan Y, Bajpai S K and Bajpai M 2007 Review on polymer, hydrogel and microgel metal nanocomposites: a facile nanotechnological approach *J. Macromol. Sci. A* **45** 107
- [52] Ahmed E M and Aggor F S 2010 Swelling kinetic study and characterization of crosslinked hydrogels containing silver nanoparticles *J. Appl. Polym. Sci.* **117** 2168
- [53] Zhang D X, Yoshikawa C, Welch N G, Pasic P, Thissen H and Voelcker N H 2019 Spatially controlled surface modification of porous silicon for sustained drug delivery applications *Sci. Rep.* **9** 1367
- [54] Zhang D, Ma Z, Spasova M, Yelsukova A E, Lu S, Farle M, Wiedwald U and Gökce B 2017 Formation mechanism of laser-synthesized iron–manganese alloy nanoparticles, manganese oxide nanosheets and nanofibers *Part. Part. Syst. Char.* **34** 1600225
- [55] De Bonis A, Lovaglio T, Galasso A, Santagata A and Teghil R 2015 Iron and iron oxide nanoparticles obtained by ultra-short laser ablation in liquid *Appl. Surf. Sci.* **353** 433
- [56] Mudunkotuwa I A, Rupasinghe T, Wu C M and Grassian V H 2012 Dissolution of ZnO nanoparticles at circumneutral pH: a study of size effects in the presence and absence of citric acid *Langmuir* **28** 396
- [57] Yoko I, Yumi K, Takako K, Kentaro Y, Hiroshi A, Chihiro M, Fumiyoshi K and Takuo O 2016 Relationship between physical parameters of various metal ions and binding affinity for alginate *Biol. Pharm. Bull.* **39** 1893
- [58] Lai Y L, Thirumavalavan M and Lee J F 2010 Effective adsorption of heavy metal ions ( $\text{Cu}^{2+}$ ,  $\text{Pb}^{2+}$ ,  $\text{Zn}^{2+}$ ) from aqueous solution by immobilization of adsorbents on Ca-alginate beads *Toxicol. Environ. Chem.* **92** 697
- [59] Jodra Y and Mijangos F 2001 Ion exchange selectivities of calcium alginate gels for heavy metals *Water Sci. Technol.* **43** 237
- [60] Pathak T S, Yun J H, Lee J and Paeng K J 2010 Effect of calcium ion (cross-linker) concentration on porosity, surface morphology and thermal behavior of calcium alginates prepared from algae (*Undaria pinnatifida*) *Carbohydr. Polym.* **81** 633
- [61] Ângela L A, José M F F and Rosana Z D 2004 Zeta potential measurement in bioactive collagen *Mater. Res.* **7** 631
- [62] Norde W 1986 Adsorption of proteins from solution at the solid-liquid interface *Adv. Colloid Interface Sci.* **25** 267
- [63] Lee A, Hudson A R, Shiwarski D J, Tashman J W, Hinton T J, Yerneni S, Bliley J M, Campbell P G and Feinberg A W 2019 3D bioprinting of collagen to rebuild components of the human heart *Science* **365** 482
- [64] Amendola V *et al* 2020 Room-temperature laser synthesis in liquid of oxide, metal-oxide core-shells, and doped oxide nanoparticles *Chem. Euro. J.* (<https://doi.org/10.1002/chem.202000686>)